Journal of
Microscopy

Journal of Microscopy, Vol. 257, Issue 2 2015, pp. 133–141 doi: 10.1111/jmi.12192
Received 10 December 2013; accepted 7 October 2014

Analysis of menisci formed on cones for single field of view parasite egg microscopy

I.R. COOKE*, C.J. LAING†, L.V. WHITE‡, S.J. WAKES‡ & S.J. SOWERBY§,‖
*Department of Chemistry, University of Otago, Dunedin, New Zealand
†Department of Mathematics and Statistics, University of Otago, Dunedin, New Zealand
‡Department of Applied Sciences, University of Otago, Dunedin, New Zealand
§Department of Biochemistry, University of Otago, Dunedin, New Zealand
‖Centre for Bioengineering and Nanomedicine, University of Otago, Dunedin, New Zealand

Key words. Meniscus, microscopy, parasite.

Summary

Parasite ova caused to accumulate in a single microscopic field simplifies monitoring soil-transmitted helminthiasis by optical microscopy. Here we demonstrate new egg-accumulating geometries based on annular menisci formed on the surface of a wetted cone. Fluidic features extracted from profile images of the system provided mathematical representations of the meniscus gradient that were compared quantitatively to numerical solutions of an axisymmetric Young–Laplace equation. Our results show that the governing dynamics of these systems is dominated by the surface tension of the fluid. These image analysis and mathematical tools provide simple quantitative methods for system analysis and optimization.

Introduction

Light microscopy remains the most widely used and versatile method for monitoring gastrointestinal parasitism in veterinary and human health. However, determining the presence of helminth ova (20–200 μm) in stool is confounded by the complex colloidal properties of faeces and deep staining due to chromophores. These challenges have traditionally been overcome by dispersing faecal material thinly across a flat transparent surface to enable sufficient light penetration for trans-illumination of the ova and to present the sample in a common focal plane for imaging (Thienpont *et al.*, 1979; Ash & Orihel, 2007).

Traditional optics used to visualize parasite eggs employ a 4× objective lens combined with a 10× eyepiece yielding 40× magnification. In this configuration, the microscopic field of view (FOV) is typically a circle of diameter 4.45 mm (area = 15.55 mm^2). However, for the close inspection often required for egg discrimination, a 10× objective lens is used to increase the magnification to 100×, but reduces the FOV to a circle of diameter 1.78 mm (area = 2.49 mm^2).

For the optical detection of eggs in stool, a number of approaches have been developed to prepare the faecal-derived material for microscopic inspection. The Kato–Katz method (Katz *et al.*, 1972), the semiquantitative human diagnostic standard of the World Health Organization (Ash *et al.*, 1994), employs a cardboard sheet incorporating a hole, which acts as a simple former to position a fixed amount of stool (approximately 43.7 mg) on a microscope slide. The sample is caused to spread over an area up to 25 mm in diameter (area = 490 mm^2), which represents 31 and 197 nonoverlapping FOV at 40× and 100× magnification, respectively.

Fluidizing stool by the addition of liquid and mechanical homogenization provides a means to randomize the distribution of eggs and permits their separation and concentration by filtration, sedimentation and flotation (Thienpont *et al.*, 1979; Ash & Orihel, 2007). Flotation of parasite ova is commonly used in coprological analysis and a number of flotation fluids have been developed (Thienpont *et al.*, 1979; Ash & Orihel, 2007; Cringoli *et al.*, 2010).

The McMaster method is a widely utilized veterinary parasite diagnostic (MAFF, 1986; Thienpont *et al.*, 1979; Cringoli *et al.*, 2004) recently adapted for human application (Levecke *et al.*, 2011; Albonico *et al.*, 2012). It comprises a pair of identical volumetric fluid chambers that facilitates the presentation of fluidized faecal samples thin enough for trans-illumination. Stool homogenized in dense fluids causes the eggs to float to the underside of a transparent window where buoyancy pins floating objects in a common focal plane for imaging. Gridlines that correspond to a total searchable area of 100 mm^2 help facilitate systematic examination of 0.15 mL of captured fluid per chamber. The volume can be increased to

Correspondence to: Stephen J. Sowerby, Department of Biochemistry, University of Otago, PO Box 56, Dunedin, New Zealand. Tel: +64 3 479 9761; fax: +64 3 479 7866; e-mail: stephen.sowerby@otago.ac.nz

© 2014 The Authors
Journal of Microscopy © 2014 Royal Microscopical Society

0.5 mL but comes with a concomitant increase in the search area to 324 mm^2 (Cringoli *et al.*, 2004; Presland *et al.*, 2005). Analysis of the paired chambers is typically used to confirm sampling consistency but doubles the microscopy burden.

The FLOTAC apparatus, like the McMaster slide, facilitates the examination of grid-lined areas of 324 mm^2, following active mechanical capture of the eggs floated atop of paired 5 mL chambers subjected to centrifugation-enhanced flotation (Cringoli *et al.*, 2010).

Systematic examination of faecal-derived material is normally done in real time (synchronous) by *skilled* technicians operating the manual translation stage of a compound optical microscope. However, the necessary colocalization of expertise and technology limits the widespread monitoring of helminthiasis.

Single FOV imaging eliminates the need for lateral translation and offers a number of advantages including: raw digital electronic capture, computer assisted analysis, remote location processing, and the ability to archive and audit data (Mes *et al.*, 2007; Sowerby *et al.*, 2011; White *et al.*, 2013).

Mes *et al.* (2007) first showed the elegant use of curved fluid interfaces (menisci) to facilitate single FOV imaging of parasite eggs caused to accumulate at an oil–water interface. The curvatures of axisymmetric menisci generated about a hydrophilic glass rod with a hemispherical terminus were used in fluid cells designed to orient interfacial pollen grains and nematode eggs for microscopic analysis (Sowerby *et al.*, 2011). Buoyant particles quantitatively introduced to the fluid cell accumulated about the apex of the rod. The rod itself had the effect of stabilizing the meniscus, enabled particle beaching about the spherical rod cap and provided a conduit for trans-illumination of the beached particles. Top view images of the trans-illuminated rod were magnified to occupy a single microscopic FOV.

These first empirical studies of particle-accumulating fluid cells (Sowerby *et al.*, 2011; White *et al.*, 2013) resulted in a meniscus generating structure that comprised a 3-mm-diameter rod concentrically located within an 8-mm well. Although the 3 mm diameter of the rod corresponded to a maximum single FOV of 7.07 mm^2, it was found that the hemispherical terminus resulted in a large unwetted central portion incorporating the apex of the hemisphere. This reduced the effective usable FOV and the operational area in system was limited to a thin annulus around the tapering end of the rod. Furthermore, the grinding of hemispherical termini is expensive and is confronted by manufacturing variance (White *et al.*, 2013).

In this paper, we address these issues by extending the single FOV microscopy approach to new configurations of the fluid cell that introduce rods with conical termini (Fig. 1). Rods with conical ends are simple geometries to manufacture and could be configured with different open angles and at different heights within the fluid cell. Using one configuration of fluid cell, we extract the meniscus gradient directly from profile

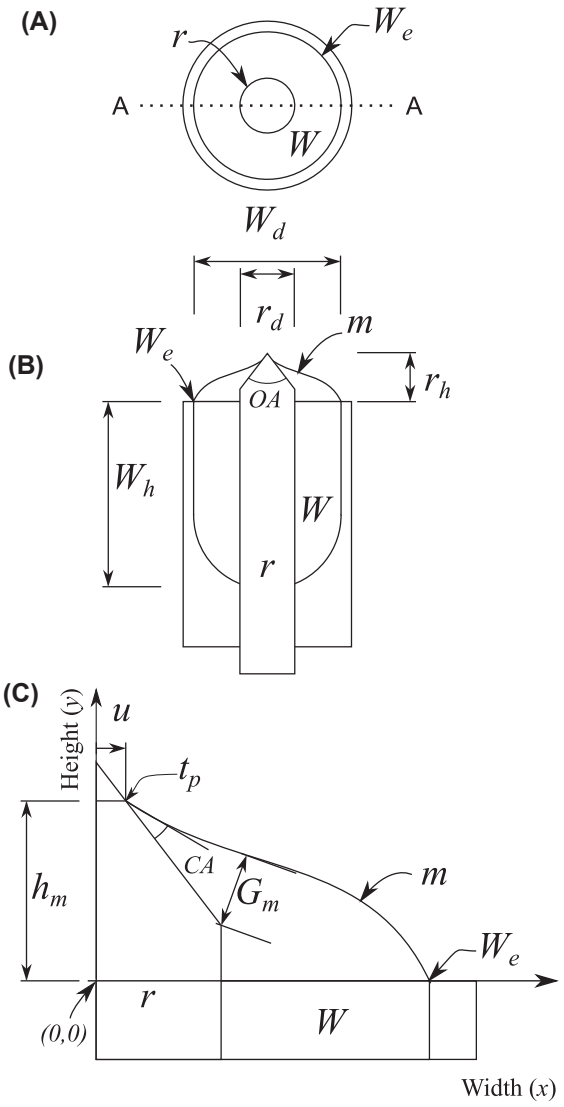

Fig. 1. Schematic of the particle-accumulating fluid cell. (A) Top view showing: rod (r), well (W) and well edge (We). (B and C) Transverse cross-sections of A along the line A-A showing: the meniscus (m), cone open angle (OA), rod diameter (rd), rod height above the well edge (rh), well diameter (Wd), well depth (Wh), the triple point (tp), contact angle on the cone surface (CA), the unwetted radius (u), the meniscus rise height (hm) and the minimum dimension between the base of the cone and the meniscus (Gm). A coordinate system based on the width (x) from the centre of the rod vs. height (y) from the well edge is shown in C.

images of the system and compare the observed gradients quantitatively with modelled gradients. Here, the goal is to develop a simple approach to characterize the key attributes governing meniscus-based fluid cell geometries to aid in their further optimization for diagnostic parasite microscopy.

Understanding of the potential utility of menisci for coprological parasite microscopy starts with the fundamental interfacial behaviour of buoyant particles. Meniscus curvature generates applied fields (Cavallaro *et al.*, 2011)

© 2014 The Authors

with a propensity to passively orient floating colloidal materials (Hu & Bush, 2005; Vassileva *et al.*, 2005; Vella & Mahadevan, 2005; Wurger, 2006; Malaquin *et al.*, 2007; Yu *et al.*, 2007; Boneva *et al.*, 2009; Rivron *et al.*, 2009; Danov & Kralchevsky, 2010; Dominguez *et al.*, 2010; Cavallaro *et al.*, 2011; Botto *et al.*, 2012). Buoyant particles cluster at interfaces due to particle-induced curvature of the meniscus between particles (Wurger, 2006; Lewandowski *et al.*, 2008; Danov & Kralchevsky, 2010). Capillary rise at the walls inside liquid-containing vessels generates menisci that facilitate circumferential particle accumulation often called the 'cheerios effect' (Vella & Mahadevan, 2005). Similar interfacial structures at pond edges permit meniscus climbing by waterborne insects (Hu & Bush, 2005; Yu *et al.*, 2007). The motion of particles trapped at curved interfaces is complex and dependent on many factors including the interplay between meniscus curvature and shape (Cavallaro *et al.*, 2011; Botto *et al.*, 2012) and between the interfacial gradient and particle buoyancy (Vassileva *et al.*, 2005).

The underpinning physical chemistry that controls meniscus curvature and particle accumulation has its origins in the cohesive and adhesive molecular–scale interactions between fluids and solids. Partial wetting of a solid with a liquid results in a triple point phase boundary between the solid, liquid and vapour phases. A characteristic contact angle (θ_γ) between the liquid–vapour and the solid–liquid interfaces arises from adhesive molecular and topological characteristics of the contacting materials. Young's equation expresses the relationship between the relevant interfacial tensions and θ_γ by

$$\cos\theta_\gamma = \frac{\gamma_{sv} - \gamma_{sl}}{\gamma_{lv}},$$

where γ_{lv}, γ_{sv} and γ_{sl} refer to the liquid–vapour, solid–vapour and solid–liquid interfacial tensions, respectively (Young, 1805).

The natural curvature of static fluids at the liquid–vapour boundary is due to shape adjustment of the liquid volume to minimize surface area and the excess energy caused by unbalanced cohesive molecular arrangements at the interface (de Gennes *et al.*, 2010).

The interplay between γ_{lv} and gravitational acceleration (g) gives rise to the capillary length (l_c), which is given by

$$l_c = \sqrt{\frac{\gamma_{lv}}{\Delta\rho g}},$$

where $\Delta\rho$ is the difference in density between the liquid and the vapour fluids. The l_c simply describes the typical linear dimension at which gravity influences the shape of the fluid curvature (de Gennes *et al.*, 2010). For water, $l_c = 0.27$ cm ($\gamma = 70$ dynes cm^{-1}, $\rho = 1$ g cm^{-3} and $g = 980$ cm s^{-2}).

To characterize the shape of a meniscus, the pressure difference (ΔP) across a liquid–vapour interface is proportional to γ_{lv} and the fluid curvature as described by the Young–Laplace (Y–L) equation:

$$\Delta P = \gamma_{lv}\left(\frac{1}{R_1} + \frac{1}{R_2}\right),$$

where R_1 and R_2 are the principal radii of curvature at any point on the interface (Young, 1805; de Laplace, 1806). The addition of $\Delta\rho g z$ to the right-hand side of Y–L equation accommodates the influence of gravity on the meniscus, where $\Delta\rho$ is the difference in density of the liquid and vapour phases, g is the acceleration due to gravity and z is the height.

The Y–L equations lack a general analytical solution due to the involvement of mixed second-order derivatives of the shape functions describing the menisci (Pozrikidis, 2010). In previous work on menisci generated by hemispherical geometries (White *et al.*, 2013), a numerical solution to the Y–L equation was obtained using the finite element method Surface Evolver (Brakke, 1996), which solves a complicated, highly nonlinear parabolic partial differential equation. In these studies, only the meniscus height and radius measurements were evaluated and there was no quantitative comparison of the modelled and observed meniscus curvature. However, the axisymmetric geometry of these systems is simple enough to reduce the problem to an ordinary differential equation of a single variable. This approach is more intuitive than Surface Evolver because the equation being solved is a height function, which depends on the radius and provides a solution that can be easily compared to the observed meniscus gradient.

Axisymmetric forms of the Y–L expression (aY–L) are reduced to a second-order nonlinear ordinary differential equation:

$$\frac{\Delta P}{\gamma_{lv}} = \left(\frac{1}{R_1} + \frac{1}{R_2}\right) = 2H = \frac{f'(r)}{r\left(f'(r)^2 + 1\right)^{1/2}} + \frac{f''(r)}{\left(f'(r)^2 + 1\right)^{3/2}},$$

where H is the mean curvature, r is the radial coordinate from the centre of the cone and f is a one-dimensional function that represents the position of the surface. With the inclusion of the gravity term, this equation becomes

$$2H = \frac{f'(r)}{r\left(f'(r)^2 + 1\right)^{1/2}} + \frac{f''(r)}{\left(f'(r)^2 + 1\right)^{3/2}} + \rho g f(r).$$

Although ΔP is in theory measurable, it is the geometrical properties of the liquid that are observed, specifically, the location of the liquid intersections with solid objects (the well edge and cone) and the liquid volume. At constant temperature, volume and pressure are related and in static fluidic systems, ΔP is in a steady state (constant). Thus, for a fixed volume, the position of the interface can be given by the Y–L equation, knowing the liquid–solid intersections. In this way, we were not confronted with finding the value of ΔP, rather the spatial extent of the surface versus its curvature for a fixed volume.

© 2014 The Authors

Fixing the volume of the liquid amounts to imposing a constraint on the aY–L equation. This can be done using the standard method of Lagrange multipliers. Determining the correct value of the Lagrange multiplier was achieved using the well-known Augmented Lagrangian method (Hestenes, 1969; Powell, 1978). The numerical solution of the aY–L equation was achieved using a fourth-order Runga–Kutta method (Dubin, 2003).

In other systems relevant to the geometry of the fluid cell, a cylindrical post rising out of a wetting liquid generates axisymmetric menisci commonly seen in wire coating (White & Tallmadge, 1965) and solder joints (Clanet & Quere, 2002). The theoretical maximum height for menisci on wetted rods of radius, r, for $\theta_\gamma = 0$, approaches l_c as $r \to \infty$ (Tallmadge, 1971). Similarly, such menisci also decay over a length comparable to l_c (Lo, 1983).

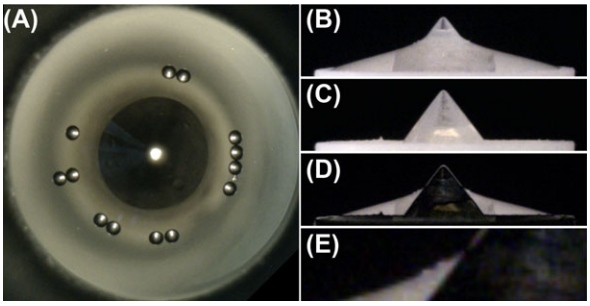

Fig. 2. Images of the apparatus. (A) Top view image of the cone (3.0 mm ø) in a fluid-filled well (500 μL) showing an annular assemblage of buoyant polystyrene particles (150 μm ø). (B) Profile image of the apparatus in A showing the cone positioned with its apex (75° open angle) 1.80 mm above the well edge. (C) Profile image of the cone in A with fluid removed. (D) Profile difference image of the cone in A created using images (B) and (C). (E) Enlarged portion of the profile difference image in D showing the fluid wedge and particle profile.

Materials and methods

Fluid cells (Fig. 1), installed in *Micro-i* cassettes from Menixis (Dunedin, New Zealand), comprise polytetrafluoroethylene wells of diameter, 8 mm diameter with a hemispherical base at depth of 12.1 mm. The wells have a 9 mm outer diameter with a square edged rim and a nominal wall thickness of 0.5 mm. In the centre of the well is a borosilicate rod lens (diameter = 3.0 ± 0.1 mm), with the top end conical, open angle = 75 ± 1° and polished (surface quality 60–40) set to 1.80 mm above the well edge. For each measurement, the rod and well were swabbed with 0.1% (w/v) sodium dodecyl sulphate, thoroughly rinsed with distilled H_2O and dried with compressed air before being filled with fluid. This regime yielded contact angles of 19 ± 2°.

For the microscopy, we used a portable *Micro-i* imager from Menixis (Dunedin, New Zealand). This imaging system incorporates a 0.8 in. (5.70 mm × 4.28 mm) colour CMOS image sensor: the pixel size is 2.2 μm × 2.2 μm arrayed in a 2592 × 1944 matrix yielding 5 Megapixel images with an aspect ratio of 4:3. The board-level camera is fitted with an achromat doublet lens and a 3-mm-diameter aperture such that the image of the 3-mm-diameter field is projected onto the image sensor at an optical magnification of approximately 1.3:1 with a working distance of approximately 20 mm. Assuming efficient optics, a 1.7-μm-long image feature is optically magnified to 2.2 μm and covers approximately one image sensor pixel. A 24 in. monitor, running at 1920 × 1440 resolution, has 100 pixels per inch; each pixel is approximately 245 μm long. Projection of the images with this monitor at 1:1 corresponds to a pixel scaling of approximately 111× (245/2.2). Combined with the optics, this results in a potential 145× magnification (1.3 × 111). In practice, the image of the 3-mm-diameter rod is scaled onto the computer screen and adjusted to 300 mm to ensure single FOV coverage when viewed by a human, corresponding to 100× magnification. Digital zoom permits further magnification at the image's native resolution of 145× magnification with the smallest eggs (20 μm) covering approximately 11 pixels on the images horizontally. Object trans-illumination occurs via a white LED under pulsed width modulation control.

For particle microscopy, 150-μm ø polystyrene beads (density = 1.05 g mL^{-1}, from Sigma-Aldrich, Auckland, New Zealand) were suspended in NaCl solution adjusted to have a specific gravity of 1.15. Fresh sheep stool samples were processed and independently analysed by a competent technician using a modified McMaster approach (Presland *et al.*, 2005) to confirm the presence and identity of helminth eggs. The samples were utilized in this study within 2 weeks of processing following dilution 1:13 using saturated NaCl solutions (specific gravity 1.20). Analyte solutions containing particles or eggs were mixed by 4–5 rounds of inversion and swirling before samples were removed by micropipette and applied to the fluid cell.

For the profile images, a fluid cell was removed from its cassette and imaged using a jury-rigged stage comprising a horizontally positioned digital camera, a pedestal for holding the well and a source of diffuse backlighting to facilitate edge definition of the meniscus. The images were ported to the public domain program ImageJ (Rasband, 2008) and calibrated using the rod diameter (3.0 mm) or the height of the cone apex above the well edge (1.80 mm) as the internal dimensional standard. Measured data were taken from the calibrated difference images (e.g. Fig. 2D), created in ImageJ using the 'Difference' option of the 'Image Calculator' on images of the empty well (Fig. 2C) and the filled wells (Fig. 2B), which enabled the meniscus edges and rod geometry to be clearly defined.

Cartesian coordinates of the meniscus edge were assigned in images cropped to have a common origin (Fig. 1C) and the edge geometry extracted from the calibrated difference images using the manually operated 'Multipoint' tool of ImageJ. The coordinate data were plotted using Microsoft Excel and

© 2014 The Authors

polynomial functions were fitted by least squares regression to generate a mathematical representation of the one-dimensional meniscus gradient. To examine the effect of fluid volume on meniscus profile, the well was filled using a micropipette with water to create a static droplet of liquid proud of the well that was stabilized by pinning at the well edges. Successive removal of fluid using a micropipette (nominally 10 μL) enabled cumulative volume changes to be made. For each volume and subsequent volume changes, the profile of the well was photographed. All experiments were performed at 22 ± 2 °C.

Assuming a perfect well and rod geometry, calculation yielded a geometric volume below the line of the well edge of 455.7 μL. However, the measured diameter of the well at the top edge was larger (8.25 ± 0.05 mm) than the 8.0 mm tool diameter used to create the well due to machining nonlinearities. Recalculation using this well diameter yields a below-edge volume of 486.2 μL. However, such machined geometries are likely to yield a tapering well, which suggests the true volume lies within the range 455–486 μL. Determination of liquid volume above the edge of the well was achieved by analysis of profile images to mitigate the unreliability of pipetting microliter volumes of liquid. The volume was calculated by integration of the fitted polynomials and rotating the two-dimensional slice representing the fluid that exists between the well edge and the wetted radius about the y-axis and subtracting the intersecting volume of the cone. The below-edge volume of the well was determined by subtraction of the calculated above-edge volume following the addition of precisely metered water to the well. In a series of replicates ($N = 10$), a pipette (calibrated by measurement of dispensed liquid mass: 541 μL, $N = 29$, SD = 2 μL) delivered 541 μL to yield a sessile droplet that sat proud of the well edge with its meniscus not interrupted by the cone (see Fig. 2A, for example). The coordinate points from the meniscus edges of all the replicates were plotted together and a polynomial fitted to the combined data by least squares regression. The calculated above-edge fluid volume (67.1 ± 2 μL), subtracted from the loaded mean total volume, yielded a below-edge volume of 473.9 ± 2 μL that was mid-way in the calculated range (455–486 μL).

Numerical solutions to the aY–L equation were obtained for each data set using a standard Runga–Kutta method with Dirichlet boundary conditions (Dubin, 2003). These conditions were obtained by extrapolating the experimental data to the intersection points of the interface with the cone and the well lip. In this system it was necessary to differentiate between surfaces attached to the cone, and surfaces that encompass it entirely. The accuracy of the experimental data was measured by taking the mean of the minimized L2-norms of the distances between each data point and the numerical solution. For data points $x_0, x_1, \ldots, x_n$, we have

$$D = \frac{\sum_{i=1}^{n} \min\left(P f\left(r\right) - x_i P_2\right)}{n},$$

in which D is the normal Euclidean distance between the measured and numerically modelled data.

Results and discussion

Empirical observations of rods with conical termini with a 75° open angle positioned 1.8 mm proud of the well edge yielded menisci useful for particle accumulation. In Figure 1, the general configuration of the fluid cell comprised a volumetric well and a centrally located rod with a conical terminus. In the top view (Fig. 1A), the conical terminus of the rod is viewed orthogonally and in operation is trans-illuminated from its base. The transverse cross-section shown in Figure 1(b) shows the key physical variables of the cell. Figure 1(C) shows the key measured attributes due to the physical–chemical properties of the system. Note that in the schematic of Figure 1, the base of the cone is diagrammatically raised more than in the experimental system.

In the top view image of the trans-illuminated cone wetted by fluid containing buoyant polystyrene microspheres (Fig. 2A), the central dark region is unwetted and shows a point of high intensity corresponding to the apex of the cone. Although liquid extends from the circular wetting line to the well edge (not shown), only the portion from the wetting line to the circumferential boundary of the rod edge constitutes the effective operational trans-illuminated area of the system. Within this annular zone, the particles beach on the rod surface in a circular configuration show a tendency to cluster and can hinder each other. Gentle vibration can disrupt the clustering and cause the particles to reassemble into different configurations, indicating that particle accumulation can be frustrated by the appearance of metastable equilibria. It is likely that the motion of these isolated particles was dominated by the one-dimensional meniscus gradient rather than its two-dimensional curvature because the particles are spherical and so coupled to the gradient by the induced monopole due to the buoyancy of the particles (Vassileva *et al.*, 2005).

In the top view image, the morphological characteristics of the meniscus are not immediately apparent. However, profile images of the liquid-filled well (Fig. 2B) clearly show the static meniscus gradient. The liquid-wetted cone appears distorted in the images (Fig. 2B) due to optical lensing by the liquid. Profile difference images created from the void (Fig. 2C) and the liquid-filled (Fig. 2B) wells mitigate the optical distortions and have the appearance of a transverse cross-section (Fig. 2D). Inspection of the difference images reveals clearly the triple point phase boundary of the wetting line, fluid rise height and unwetted diameter.

Particles seen in the top view image (Fig. 2A) can occasionally be resolved in the profile difference images (Figs. 2D,E) and suggest a meniscus gradient induced by the particles. These observations indicate that geometric bridging by the particles between the cone surface and the liquid–vapour interface limits the distribution of particles and the annular liquid wedge

© 2014 The Authors

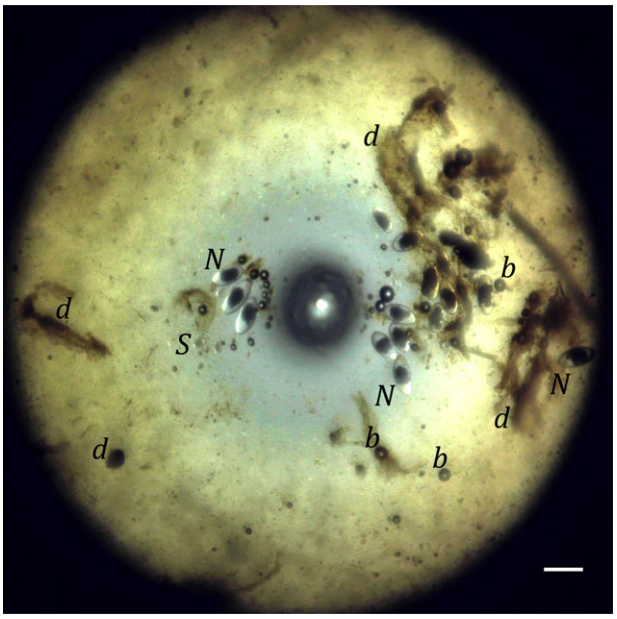

Fig. 3. Top view image of the apparatus showing the cone (3.0 mm ø) in a fluid-filled well. Marked in the figure are: d, debris; b, air bubbles; N, Nematodirus; S, Strongyle eggs. The scale bar (lower left) is 200 μm.

morphology accounts for the circular distributions particles at a common radius. These also suggest a limit on the size of particle that can enter the wedge. The minimum dimension of this gating area is shown in Figure 1(C) as the length G_m, which can be found by minimizing the distance function from a general point on the meniscus to the base of the cone.

In Figure 3, helminth ova can be seen in top view images of the cone when the fluid cell contains liquid prepared from the stool of sheep infected with *Nematodirus* and *Strongyle* parasites. The *Nematodirus* eggs can be easily distinguished from opaque debris and spherical air bubbles as the translucent ovoid structures (approximately 200 × 70 μm) that contain a dark centre. Smaller *Strongyle* eggs are also visible (60 × 30 μm). The equilibration of the eggs into an annular configuration is presumably restricted by mechanical barriers due to the confounding debris in stool. The staining of the fluid is evident from the change in colour as a function of fluid depth between the centre and circumferential edge of the cone. It is likely that the motion and equilibrium positioning of the helminth eggs will be influenced by the meniscus two-dimensional curvature due to the induced quadrapole of ellipsoid geometries (Cavallaro *et al.*, 2011; Botto *et al.*, 2012). In Figure 3, the cone apex and wetting line are resolved, but the unwetted part of the cone is much smaller than that shown in Figure 2(A) and the effective operational area of the system encompasses almost the entire area of the cone surface.

To analyse the fluidic structure, we acquired profile images of the system containing different volumes of liquid and, using images of the unfilled system, generated their accompanying difference images (Fig. 4). We manually extracted the interfacial liquid–vapour gradient from selected difference images into a common (x, y) coordinate system (see Fig. 1C) and then plotted the data (Fig. 5). Polynomials were fitted to the data and using calculus we determined the volume of liquid above the well edge.

The data extracted from the images (Fig. 4) and from plots (Fig. 5) are summarized in Table 1. From the images, the gross morphology of the meniscus at above-edge volumes >38 μL takes on a distinctly convex shape (Figs. 4A–H), whereas at volumes <18 μL the shape is concave (Figs. 4M–P). The intervening volumes can be characterized by a transition in which both convex and concave features are simultaneously present in the curvature (Figs. 4I–L) and presumably separated by a point of inflection, which shifts towards the well edge with the incremental reduction in volume. These observations are consistent with the previously observed system based on a hemispherical topology (White *et al.*, 2013).

In previous studies of hemispherical rod geometries using Surface Evolver, only fluid–solid intersection points (meniscus height and unwetted radius) were compared between measured and modelled data (White *et al.*, 2013), here we extract the meniscus gradient and quantitatively compare it to the computed model.

We calculated solutions for the aY–L with and without the accompanying gravity term. We used experimentally measured meniscus fluid–solid intersection points for the equation variables and then compared the computed solutions with the meniscus gradient data extracted from the difference images (Fig. 5 and Table 1). The mean of the distances between the aY–L solution that included gravity and the experimental data were calculated to be in the range 0.004–0.005 mm (Table 1). These comparisons show that numerical solutions to the aY–L equation closely reflect the experimentally determined meniscus gradient and suggest only minor errors in meniscus edge plotting. The mean of the distances between the aY–L solution without the gravity term and the experimental data were calculated to be in the range 0.05–0.004 mm (Table 1) and showed a maximum deviation in the order of 1%. These showed that there was only a minor but increasing effect of gravity on the meniscus gradient with increasing volume.

It is evident from Figure 5 that edge pinning becomes important at volumes >38 μL because the visible, above-edge meniscus extends to the vicinity of the well edge and the droplet starts to bulge and adopt a convex morphology. As the contact angle remains constant, the triple point moves so that the liquid volume minimizes its surface area to accommodate the volume change. Further analysis of the data in Table 1 shows that the length of the unwetted radius responds predictably to the change in volume over the range 0–50 μL, permitting volumetric assessment from the top view images by measurement of the unwetted portion as previously shown in White *et al.* (2011).

© 2014 The Authors

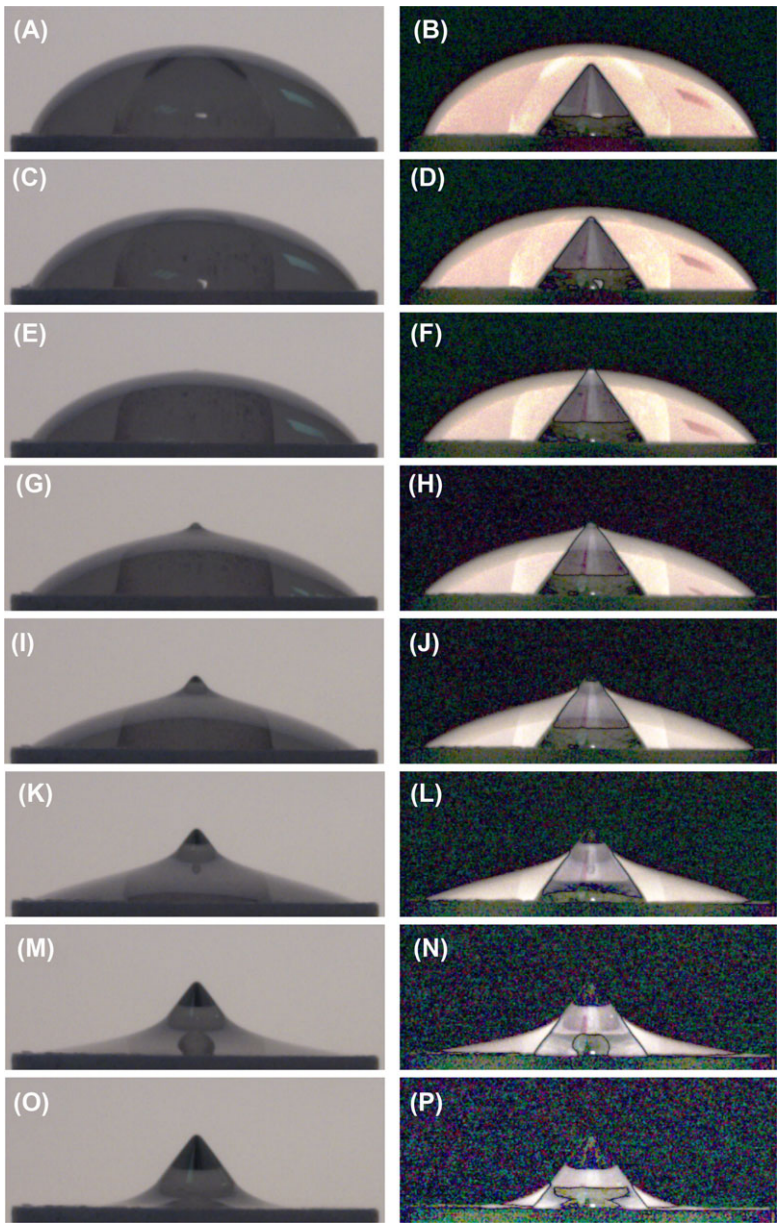

Fig. 4. Profiles of a wetted cone and their accompanying difference images with decreasing above-edge fluid volumes (μL): (A, B) 68, (C, D) 59, (E, F) 49, (G, H) 39, (I, J) 28, (K, L) 18, (M, N) 10 and (O, P) 2.

In the analysis of the factors governing the meniscus, the distance between the base of the cone and well edge was 0.25 cm. This separation is below the capillary length of water (l_c =0.27 cm) and meniscus gradients shorter than the capillary length should be unaffected by gravity. For above-edge volumes of fluid that are not obviously pinned by the well edge, the fluidic structure remains below l_c. However, as fluid volume increases, the meniscus gradient lengthens as the liquid both rises up the cone and becomes pinned at the well edge. The aY–L solution that contains no gravity term demonstrates the influence of gravity quantifiably by the measured deviation of the modelled from experimental values as expressed by the mean difference between them (Table 1).

For volumes >58 μl, sufficient liquid volume causes the meniscus to breach the apex of the cone and flattening of the liquid is observed. These systems are undesirable for particle microscopy because particle beaching does not occur and the system is prone to shear indicating decreasing stability. This propensity to shear underpins an unmetered fluid loading approach (White *et al.*, 2013) and shows that at these volumes the governing dynamics of the droplet are dominated by gravity.

© 2014 The Authors

Table 1. Summary of meniscus data and calculation.

Vol_m (μl)	Rad_m (mm)	h_m (mm)	u (mm)	a	b	c	m	D_{-g} (mm)	D_{+g} (mm)
68.1	4.12	2.28	–	−0.0404	0. 0839	−0.2028	2.33	0.039	0.005
57.6	4.12	2.01	–	−0.0308	0.0468	−0.1599	2.06	0.031	0.005
48.8	4.10	1.79	0.19	−0.0282	0.0566	−0.1950	1.83	0.030	0.005
38.6	4.10	1.70	0.21	−0.0230	0.0662	−0.3079	1.73	0.015	0.005
28.4	4.04	1.63	0.24	−0.0238	0.1220	−0.5070	1.63	0.012	0.005
18.2	3.98	1.24	0.54	−0.0280	0.2002	−0.7509	1.56	0.009	0.005
9.5	3.74	0.84	0.83	−0.0351	0.2978	−1.0304	1.52	0.007	0.004
1.9[a]	2.70	0.56	1.05		0.2449	−1.2247	1.54	0.005	0.004

Vol_m is the meniscus volume above the well edge. Rad_m is the radius of the meniscus at the well edge.
h_m is the height of the meniscus. u is the maximum radius of the unwetted portion of the cone. a, b and c are the coefficients of x^3, x^2 and x, respectively, and m is the x-axis intercept for the polynomials fitted to the experimental data. D_{-g} is the mean distance between the experimental data and the Young–Laplace equation calculated without the gravity term. D_{+g} is the mean distance between the experimental data and the Young–Laplace equation calculated with the gravity term.
[a]Fitted to second-order polynomial.

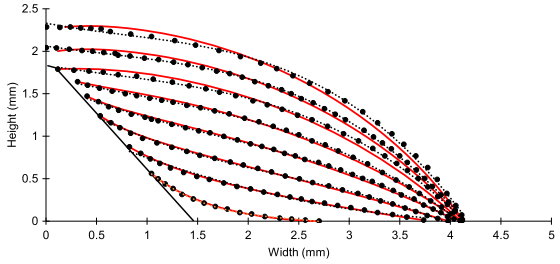

Fig. 5. Plots of meniscus gradient. The coordinate data of the menisci taken from the images in Figure 2 (black points); fitted polynomials to the coordinate data (dotted line); axisymmetric Young–Laplace calculations without gravity term (red solid line); and the underlying cone (black solid line). The calculated above-edge volumes in descending order (μL): 68, 59, 49, 39, 28, 18, 10 and 2.

These data also show that for fluid volumes <50 μL, where the cone emerges through the meniscus, the governing dynamics of this system are dominated by surface tension. In these configurations, the gradient of the meniscus is steeper and the fluid wedge thinner due to the concavity, which is presumably advantageous for particle accumulation. Furthermore, it can be seen from the above-edge well volumes that the range of 20–50 μL would confer practically useful FOV for parasite egg imaging because the annular wetted fraction of the 3-mm-diameter FOV (7.07 mm^2) corresponds to approximately 0.55–0.98, respectively.

In comparison to previous studies of the meniscus fluid–solid intersection points on hemispherical rod geometries (White *et al.*, 2013), we have demonstrated an intuitive mathematical analysis of the meniscus gradient. We have introduced a new rod geometry based on a cone and quantified the accuracy of our calculated meniscus gradients by measuring their deviation from the gradients extracted from profile images of menisci. We have included an analysis of the effect of gravity on the menisci gradients, which was shown to be minor.

Conclusions

Conically terminated rods configured to emerge through a liquid–air interface and create a meniscus, exhibit a number of advantages over previously studied hemispherical rods. These include simplified and less expensive manufacturing and a wide variety of geometric options. From the experimental observations and the aY–L calculations, the factors governing meniscus formation and liquid wedge morphology within the effective operational parameters of the fluid cell are dominated by the geometric configuration of the system, the volume of applied liquid and the surface tension of the fluid.

For quantitative microscopic applications, the well depth is independent of the meniscus and can be modulated to optimize the analytical liquid volume. These properties do not preclude the application of narrower cells, but do suggest limits on the effectiveness of much wider geometries due to the constraints imposed by the liquid surface tension. It follows that different fluids may require optimization and calibration because of the fluid cell dependency on surface tension.

Meniscus generating fluid cell structures of the type presented here are useful for single FOV microscopy of parasite eggs from stool. With these methods, future studies will be focused on testing other simple and more sophisticated geometries and further understanding the complex interfacial chemistry of fluidized stool for diagnostic microscopy.

Acknowledgements

We thank Mike Paulin, Jörg Frauendiener and George Petersen for helpful advice. This work was supported by summer studentships (I.R.C. and L.V.W.) from the Department of Applied Sciences and the Centre for Bioengineering and Nanomedicine, University of Otago; doctoral scholarship from the University of Otago (C.J.L.); funded by a grant from the Bill & Melinda Gates Foundation through the Grand Challenges

© 2014 The Authors

Explorations initiative (S.J.S.). We gratefully acknowledge Techion Group (Dunedin, New Zealand) for performing the sheep faecal analysis and the helpful comments of anonymous reviewers.

References

Albonico, M., Ame, S.M., Vercruysse, J. & Levecke, B. (2012) Comparison of the Kato-Katz thick smear and McMaster egg counting techniques for monitoring drug efficacy against soil-transmitted helminths in schoolchildren on Pemba Island, Tanzania. *Trans. R. Soc. Trop. Med. Hyg.* **106**, 199–201.

Ash, L.R. & Orihel, T.C. (2007) *Ash & Orihel's Atlas of Human Parasitology*. American Society of Clinical Pathologists Press, Chicago.

Ash, L.R., Orihel, T.C. & Savioli, L. (1994) *Bench Aids for the Diagnosis of Intestinal Parasites*. World Health Organization, Geneva.

Boneva, M.P., Danov, K.D., Christov, N.C. & Kralchevsky, P.A. (2009) Attraction between particles at a liquid interface due to the interplay of gravity- and electric-field-induced interfacial deformations. *Langmuir* **25**, 9129–9139.

Botto, L., Lewandowski, E.P., Cavallaro, M. & Stebe, K.J. (2012) Capillary interactions between anisotropic particles. *Soft Matter* **8**, 9957–9971.

Brakke, K.A. (1996) The surface evolver and the stability of liquid surfaces. *Philos. Trans. R. Soc. A* **354**, 2143–2157.

Cavallaro, M., Botto, L., Lewandowski, E.P., Wang, M. & Stebe, K.J. (2011) Curvature-driven capillary migration and assembly of rod-like particles. *Proc. Natl. Acad. Sci. U S A* **108**, 20923–20928.

Clanet, C. & Quere, D. (2002) Onset of menisci. *J. Fluid. Mech.* **460**, 131–149.

Cringoli, G., Rinaldi, L., Veneziano, V., Capelli, G. & Scala, A. (2004) The influence of flotation solution, sample dilution and the choice of McMaster slide area (volume) on the reliability of the McMaster technique in estimating the faecal egg counts of gastrointestinal strongyles and *Dicrocoelium dendriticum* in sheep. *Vet. Parasitol.* **123**, 121–131.

Cringoli, G., Rinaldi, L., Maurelli, M.P. & Utzinger, J. (2010) FLOTAC: new multivalent techniques for qualitative and quantitative copromicroscopic diagnosis of parasites in animals and humans. *Nat. Protoc.* **5**, 503–515.

Danov, K.D. & Kralchevsky, P.A. (2010) Capillary forces between particles at a liquid interface: general theoretical approach and interactions between capillary multipoles. *Adv. Colloid Interface Sci.* **154**, 91–103.

de Gennes, P.G., Brochard-Wyart, F. & Quere, D. (2010) *Capillarity and Wetting Phenomena: Drops, Bubbles, Pearls, Waves*. Springer, New York.

de Laplace, P.S. (1806) *Supplément à la théorie de l'action capillaire*. Courcier, Paris.

Dominguez, A., Oettel, M. & Dietrich, S. (2010) Dynamics of colloidal particles with capillary interactions. *Phys. Rev. E Stat. Nonlin. Soft Matter Phys.* **82**, 011402.

Dubin, D. (2003) *Numerical and Analytical Methods for Scientists and Engineers using Mathematica*. Wiley-Interscience, New Jersey.

Hestenes, M.R. (1969) Multiplier and gradient methods. *J. Optim. Theor. Appl.* **4**, 303–320.

Hu, D.L. & Bush, J.W.M. (2005) Meniscus-climbing insects. *Nature* **437**, 733–736.

Katz, N., Chaves, A. & Pellegrino, J. (1972) A simple device for quantitative stool thick-smear technique in Schistosomiasis mansoni. *Rev. Inst. Med. Trop. Sao Paulo* **14**, 397–400.

Levecke, B., Behnke, J.M., Ajjampur, S.S.R., *et al*. (2011) A comparison of the sensitivity and fecal egg counts of the McMaster egg counting and Kato-Katz thick smear methods for soil-transmitted helminths. *PLoS Neglect. Trop. D* **5**, e1201. doi: 10.1371/journal.pntd.0001201.

Lewandowski, E.P., Bernate, J.A., Searson, P.C. & Stebe, K.J. (2008) Rotation and alignment of anisotropic particles on nonplanar interfaces. *Langmuir* **24**, 9302–9307.

Lo, L.L. (1983) The meniscus on a needle—a lesson in matching. *J. Fluid Mech.* **132**, 65–78.

MAFF (1986) *Manual of Veterinary Parasitological Laboratory Techniques*, Her Majesty's Stationary Office, London.

Malaquin, L., Kraus, T., Schmid, H., Delamarche, E. & Wolf, H. (2007) Controlled particle placement through convective and capillary assembly. *Langmuir* **23**, 11513–11521.

Mes, T.H.M., Eysker, M. & Ploeger, H.W. (2007) A simple, robust and semi-automated parasite egg isolation protocol. *Nat. Protoc.* **2**, 486–489.

Powell, M.J.D. (1978) A fast algorithm for nonlinearly constrained optimization calculations. *Numerical Analysis* (ed. by G. A. Watson), pp. 144–147. Springer, Berlin Heidelberg.

Pozrikidis, C. (2010) Computation of three-dimensional hydrostatic menisci. *IMA J. Appl. Math.* **75**, 418–438.

Presland, S.L., Morgan, E.R. & Coles, G.C. (2005) Counting nematode eggs in equine faecal samples. *Vet. Rec.* **156**, 208–210.

Rasband, W.S. (2008) *ImageJ U. S.* National Institutes of Health, Bethesda. Available from: http://rsb.info.nih.gov/ij/. 1997–2011. Accessed February 2011.

Rivron, N.C., Rouwkema, J., Truckenmuller, R., Karperien, M., De Boer, J. & Van Blitterswijk, C.A. (2009) Tissue assembly and organization: developmental mechanisms in microfabricated tissues. *Biomaterials* **30**, 4851–4858.

Sowerby, S.J., Mirams, G.J., Hill, P.C. & Paulin, M.G. (2011) An axisymmetric meniscus converges particles for microscopy. *J. Microsc.* **244**, 230–234.

Tallmadge, J.A. (1971) Properties of static menisci on cylinders—analytical expressions for curvature and height at contact. *J. Colloid Interf. Sci.* **37**, 801–810.

Thienpont, D., Rochette, F. & Vanparijs, O.F.J. (1979) *Diagnosing Helminthiasis through Coprological Examination*. Janssen Research Foundation, Beerse, Belgium.

Vassileva, N.D., van den Ende, D., Mugele, F. & Mellema, J. (2005) Capillary forces between spherical particles floating at a liquid-liquid interface. *Langmuir* **21**, 11190–11200.

Vella, D. & Mahadevan, L. (2005) The "Cheerios effect." *Am. J. Phys.* **73**, 817–825.

White, D.A. & Tallmadge, J.A. (1965) Static menisci on outside of cylinders. *J. Fluid Mech.* **23**, 325–336.

White, L.V., Cooke, I.R., Wakes, S.J. & Sowerby, S.J. (2013) Quantitative particle microscopy in self-metered fluids. *J. Microsc.* **250**, 159–165.

Wurger, A. (2006) Curvature-induced capillary interaction of spherical particles at a liquid interface. *Phys. Rev. E Stat. Nonlin. Soft Matter Phys.* **74**. DOI:10.1103/PhysRevE.74.01402.

Young, T. (1805) An essay on the cohesion of fluids. *Philos. T. R. Soc. Lond.* **95**, 65–87.

Yu, Y., Guo, M., Li, X. D. & Zheng, Q.S. (2007) Meniscus-climbing behavior and its minimum free-energy mechanism. *Langmuir* **23**, 10546–10550.

© 2014 The Authors